

## FULL ARTICLE

# In vivo metabolic imaging and monitoring of brown and beige fat

Sicong He<sup>1,2</sup> | Yitai An<sup>2,3</sup> | Xuesong Li<sup>1,2</sup> | Xiuqing Wei<sup>2,3</sup> | Qiqi Sun<sup>1,2</sup> | Zhenguo Wu<sup>2,3\*</sup> | Jianan Y. Qu<sup>1,2\*</sup><sup>1</sup>Department of Electronic and Computer Engineering, Hong Kong University of Science and Technology, Kowloon, Hong Kong<sup>2</sup>Center of Systems Biology and Human Health, Hong Kong University of Science and Technology, Kowloon, Hong Kong<sup>3</sup>Division of Life Science, State Key Laboratory of Molecular Neuroscience, Hong Kong University of Science and Technology, Kowloon, Hong Kong**\*Correspondence**

Zhenguo Wu, Division of Life Science, State Key Laboratory of Molecular Neuroscience, Hong Kong University of Science and Technology, Clear Water Bay, Kowloon, Hong Kong.

Email: bczgwu@ust.hk

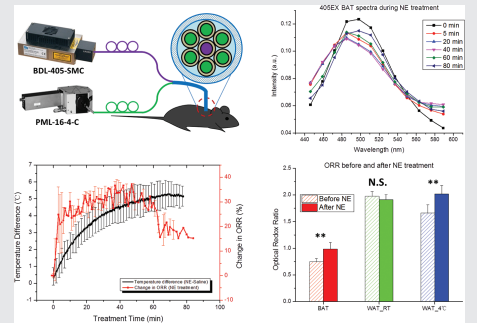
Jianan Y. Qu, Department of Electronic and Computer Engineering, Hong Kong University of Science and Technology, Clear Water Bay, Kowloon, Hong Kong.

Email: eequ@ust.hk

**Funding information**

Hong Kong Research Grants Council, Grant/Award Number: 662513, 16103215, 16148816, T13-607/12R and T13-706/11-1, AOE/M-09/12; Hong Kong University of Science and Technology, Grant/Award Number: RPC10EG33

Activation of the thermogenic brown and beige fat is an effective means to increasing whole-body energy expenditure. In this work, a unique label-free method was developed to quantitatively assess the metabolism and thermogenesis of mouse adipose tissues in vivo. Specifically, an optical redox ratio (ORR) based on the endogenous fluorescence of mitochondrial metabolic coenzymes (nicotinamide adenine dinucleotide and flavin adenine dinucleotide) was used to measure the metabolic state of adipocytes. Our findings demonstrate that the ORR provides a label-free and real-time biomarker to determine the thermogenic response of brown, beige and white adipose tissues to a variety of physiological stimulations. In addition, the redox ratio also can be used to evaluate the degree of browning in the white fat of cold-acclimated mice. This technique is important to understand the recruitment and activation of thermogenic adipocytes in mammals and thus can help to develop therapeutic strategies against obesity.

**KEYWORDS**

beige fat, metabolism, multiphoton microscopy, optical redox ratio, spectroscopy, thermogenesis

## 1 | INTRODUCTION

The fundamental cause of obesity is the chronic imbalance between energy intake and consumption. Adipose tissue plays an essential role in energy storage and expenditure in human body [1]. However, adipose tissue dysfunction is a key factor in the development of obesity-related chronic diseases, such as diabetes mellitus type 2 and cardiovascular diseases [2–4]. There are 2 major types of fat tissues in mammals with diametrically opposing functions: white

adipose tissue (WAT) and brown adipose tissue (BAT). WAT stores the excess energy in the form of triacylglycerol to regulate energy homeostasis, while BAT dissipates energy as heat via thermogenesis [1, 5]. In 2009, independent research teams demonstrated that the thermogenically active BATs existed in human adults [6–9]. A new type of energy-burning tissue, known as beige fat, was discovered in specific WAT depots [5, 10]. The beige adipocytes could be induced in WAT depots through complex processes and exhibit similar thermogenic functions to BAT when stimulated [5, 11]. The recruitment and activation of these human

Sicong He and Yitai An contributed equally to this work.

brown and beige adipocytes may therefore constitute new approaches to increasing whole-body energy expenditure and thus developing novel therapies against obesity [12].

Brown adipocytes, the functional cell type in BAT, generate heat to maintain thermal homeostasis through nonshivering thermogenesis. This process is mediated by a specialized mitochondrial protein known as uncoupling protein 1 (UCP1). UCP1 is a specific brown adipocyte marker that regulates the thermogenic process in BAT by uncoupling oxidative phosphorylation from adenosine triphosphate (ATP) production. UCP1 can induce a proton leak across the inner membrane of mitochondria and dissipate the inner mitochondrial membrane potential [1, 13]. The energy stored in the proton-motive force is released as heat. As reported previously, the thermogenesis in BAT can account for over 60% of the total energy expenditure of the mouse, indicating the enormous effect of BAT on the whole-organism metabolism [14, 15]. Aside from significant differences in functionality, brown adipocytes can also be clearly differentiated from white adipocytes by their distinct morphologies. White adipocytes are filled with 1 large lipid droplet surrounded by a thin layer of cytoplasm, while brown adipocytes contain large numbers of smaller lipid droplets and a cytoplasm packed with numerous mitochondria containing UCP1 [5].

The metabolic status of adipocytes is an important indicator for understanding and evaluating the thermogenic capacity of adipose tissues. The oxygen consumption rate of either isolated mouse adipocytes or entire mice is commonly used to measure the thermogenic metabolism of adipose tissues [16, 17]. However, for *in vivo* applications in live mice, the oxygen consumption of a whole mouse cannot accurately reflect the metabolic activity of specific adipose depot. As the traditional metabolic analyses suffer from poor spatial resolution and low specificity, the metabolic characteristics of the adipose tissue at different depots during thermogenesis thus remain unclear. Therefore, it is highly desirable to develop a method for measuring the metabolic rate of adipocytes *in vivo* at high spatial and temporal resolutions.

It is well known that the cellular coenzymes-reduced nicotinamide adenine dinucleotide (NADH) and flavin adenine dinucleotide (FAD), 2 major endogenous fluorophores, play significant roles in the mitochondrial electron transport chain (ETC). Their autofluorescence are widely used as intrinsic fluorescence biomarker to measure the metabolisms of cells and tissues *in vivo* [18–20]. Specifically, the relative fluorescence intensity NADH/FAD, defined as the optical redox ratio (ORR), can be used to evaluate the oxidation–reduction ratio of the mitochondrial matrix space and enables the sensitive and label-free probing of the cellular redox state [21–23]. Strong correlations between the ORR and cellular metabolic activities, such as oxygen consumption and glycolysis rates, have

been reported [24, 25]. In terms of the metabolism of adipocytes, NADH and FAD are highly involved in mitochondrial fatty acid  $\beta$ -oxidation, which is the catabolic process of fatty acid molecules and plays a significant role in the energy dissipation of brown adipocytes [26, 27]. The fatty acid molecules are broken down in the mitochondria to generate acetyl-CoA that enters the citric acid cycle. During this process, NADH and FADH<sub>2</sub> are formed through the reduction of NAD<sup>+</sup> and FAD, respectively, and then involved in the ETC to produce ATP or generate heat [5]. Since only the NADH and FAD are fluorescent, the ORR can be used to measure the production and consumption of these 2 molecules and characterize the cellular redox state in the process of  $\beta$ -oxidation. This may provide a unique label-free approach to facilitate the understanding of the metabolic activities of adipocytes in thermogenesis.

Recently, a study of endogenous fluorescence in adipose tissues was reported [28]. However, the correlation between the endogenous fluorescence and thermogenesis of brown and beige fat was not studied because the *in vitro* study was conducted in excised tissue samples. In this work, we investigate the metabolic characteristics of different types of adipocytes in mice during adrenergically stimulated thermogenesis *in vivo*. The rise in temperature of the adipose tissue, revealed through thermal imaging, confirms that intensive thermogenesis is successfully activated by norepinephrine (NE) treatment. Using a multimodal nonlinear optical (NLO) microscope system, we conduct high-resolution functional imaging of fat tissues and characterize the redox states of brown and white adipocytes on live mice. Moreover, we develop a fiber-based spectroscopy technology to measure the thermogenic dynamics in deep adipose tissues. The study of both NLO imaging and fiber-based spectroscopy shows a rapid increase of ORR in BAT after NE treatment, indicating that the ORR is a sensitive and robust biochemical marker for assessing the thermogenesis of local adipocytes *in vivo*. Furthermore, we find that the redox rates of WAT show significantly different responses to NE in mice kept at room temperature (RT) and at 4°C cold-acclimation. This reveals the contribution of cold-induced beige adipocytes to thermogenesis and provides a label-free method to measure the local metabolism at high spatial resolution in the highly heterogeneous browning WAT *in vivo*. Meanwhile, a correlation between the UCP1 expression and the basal ORRs confirms that the ORR is a highly sensitive marker for evaluating the degree of WAT browning in cold-acclimated mice. The technologies developed in this work enable the quantitative and label-free probing of the metabolic characteristics of adipose tissues *in vivo*, which provides unprecedented insight into the biomedical functions of the newly discovered beige fat.

## 2 | METHODS AND MATERIALS

### 2.1 | Animals

The C57BL/6J mice model was used in this study. Unless stated, mice were kept at RT. For cold experiments, 2-month-old male mice were housed at 4°C for 25 to 30 days to achieve full cold-acclimation [29]. During the experiments, mice were anesthetized through an intraperitoneal injection of ketamine (0.1 mg/g of body weight) in combination with xylazine (0.01 mg/g of body weight). Mouse skin was removed from the interscapular or inguinal region to leave an imaging window of about 2 cm<sup>2</sup>. Mice were given an intraperitoneal injection of NE (A7257; Sigma-Aldrich, St. Louis, Missouri, USA, 1 µg/g of body weight) or saline. After live imaging experiments, mice were sacrificed through cervical dislocation. The study was approved by the Animal Ethics Committee of Hong Kong University of Science and Technology.

### 2.2 | In vivo thermal imaging of adipose tissues

An infrared camera (SC7000; FLIR Systems, Wilsonville, Oregon, US) mounted with a lens (L0106; FLIR Systems) with a focal length of 50 mm was used for the in vivo thermal imaging of adipose tissues of mice. After surgical removal of skin, the anesthetized mice were placed dorsal or ventral-side-up onto a cage for thermal imaging of BAT and WAT, respectively. The frame rate of thermal imaging was 1 frame/s. After 5 minutes of thermal imaging, the mice were injected with NE (1 µg/g of body weight) or saline with a single-use intravenous infusion needle. The intravenous infusion needle was embedded intraperitoneally prior to thermal imaging, so that the injection process would not disturb the thermal imaging procedure. After imaging, the thermal images were analyzed using Altair (FLIR Systems) to obtain the time-lapse temperature curves of the adipose tissues. Regions of interest (ROI) were selected in the interscapular or inguinal region of each mouse with an identical size of 30 mm<sup>2</sup>. The average temperature in the ROI of each thermal image was calculated to plot the temperature profile.

### 2.3 | The integrated multimodal NLO microscope system

The multimodal NLO microscope system integrated two-photon excited fluorescence (TPEF) and stimulated Raman scattering (SRS) imaging modalities. Briefly, for SRS imaging, a pump-laser-integrated optical parametric oscillator system (*pico*Emerald S; APE, Berlin, Germany) was used as the light source. The Stokes beam (1031 nm, 2.1 picoseconds, 80-MHz repetition rate) was modulated at 20 MHz and the pump beam (1.9 picoseconds, 80-MHz repetition rate) was tunable from 780 to 960 nm to sweep the SRS spectra. For the SRS imaging of lipid droplets in adipocytes, the differential wavenumber of the pump-Stokes beams was

2863 cm<sup>-1</sup>, matching the CH<sub>2</sub> stretching vibrational frequency of lipids [30]. A water immersion objective (XLPLN25XWMP2, 1.05 NA; Olympus, Tokyo, Japan) was used to focus the pump-Stokes beams onto the sample. The backscattered polarization-scrambled SRS signal was collected by the same laser-focusing objective and reflected onto a photodiode (S3590-08; Hamamatsu, Japan) through a polarizing beam splitter (PBS) cube (PBS252; Thorlabs, Newton, New Jersey, USA) [31]. A filter set (#86-108, short pass at 975 nm OD4; Edmund Optics, Barrington, New Jersey, USA; FF01-850/310; Semrock, Rochester, New York, USA) was used in front of the photodiode to block the Stokes beam and transmit the pump beam. A high-frequency lock-in amplifier (APE, Berlin, Germany) was used to demodulate the SRS signal. The output of the lock-in amplifier was imported into an acquisition card (PCIe-6363; National Instruments, Austin, Texas) to reconstruct the SRS image. In the TPEF imaging modality, a femtosecond Ti:sapphire laser with a pulse duration of 140 femtoseconds (Chameleon Ultra II; Coherent, Santa Clara, California) was tuned at 740 nm to excite individual NADH fluorescence, or 810 nm to excite the NADH and FAD signals simultaneously. The femtosecond laser was changed from p-polarization to s-polarization with a half-wave plate (SAHWP05M-1700; Thorlabs, Newton, New Jersey, USA) and combined with picosecond lasers through a PBS cube (PBS252; Thorlabs, Newton, New Jersey, USA). The backward TPEF signal was collected by the objective and reflected onto a fluorescence detection system by a dichroic mirror (FF665-Di02; Semrock, Rochester, New York, USA). In the fluorescence detection system, a spectrograph equipped with a linear array of 16 Photomultiplier tubes (PMTs) (PML-16-C-1; Becker & Hickl, Berlin, Germany) was used to record NADH and FAD signals simultaneously. The spectrograph detected light of wavelength ranged from 403 to 598 nm with 13 nm resolution. A pair of galvanometer scanners was used to scan the laser beams to generate SRS and TPEF images. The laser powers used for SRS imaging were 20 and 40 mW for pump and Stokes lasers, respectively. For the TPEF imaging, the power of the femtosecond laser was 15 mW.

### 2.4 | The fiber-based spectroscopy system for ORR measurement in deep adipose tissues

A 405-nm picosecond diode laser (BDL-405-SMC; Becker & Hickl, Berlin, Germany) was used to simultaneously excite the NADH and FAD fluorescence from adipose tissues. A multi-optical-fiber catheter was used to deliver laser light and collect the fluorescence signal. The distal tip of this catheter consists of 7 individual optical fibers. Each fiber was 200 µm in diameter and the numerical aperture was 0.22. A 1.0-mm-thick quartz window was embedded at the top of the catheter to match the refractive index of the optical fibers. The excitation laser was

delivered through the central fiber, producing a 0.5-mm diameter laser spot at the end of the catheter. The fluorescence signal was collected through the 6 fibers surrounding the central fiber. The diameter of the collection area was 1.0 mm. The distal tip was kept in gentle contact with the tissue surface during measurement. This ensured that the geometry of the illumination and collection remained constant regardless of the measurement site. The emitted fluorescence signal was directed through the 6 collector fibers into a spectrograph equipped with a linear array of 16 PMTs (PML-16-C-1; Becker & Hickl, Berlin, Germany). TPEF signals ranged 420 to 615 nm were recorded in 16 consecutive spectral bands at a 13-nm resolution. In this study, the power of the 405-nm laser on the tissue surface was 10  $\mu$ W and the integration time used for the acquisition of the auto-fluorescence signal was set as 4 seconds.

## 2.5 | Monte Carlo simulation

The Monte Carlo simulation was performed using an open-source virtual tissue simulator toolkit (Virtual Photonics Technology Initiative, National Institutes of Health, Bethesda, Maryland, USA) [32]. The photons were launched from a Gaussian source with beam diameter of 0.5 mm. The absorption coefficient,  $\mu_a$ , and transport scattering coefficient,  $\mu'_s$ , of subcutaneous adipose tissue were determined by a previous study of optical properties in adipose tissues [33]. The optical penetration depth was estimated based on the absorption and scattering parameters of adipose tissue [34]. The illuminated tissue volume was calculated as the volume irradiated at 10% to 100% of the max intensity [35, 36].

## 2.6 | Western blotting of fat biopsy

Fat specimens were isolated from mouse inguinal WAT (iWAT) and manually homogenized in a glass tissue homogenizer. The sample suspension was lysed in a lysis buffer (50 mM Tris at pH 7.4, 10% glycerol, 1% Triton X-100, 150 mM NaCl, 1 mM ethylene glycol tetraacetic acid (EGTA), 1.5 mM  $MgCl_2$ , 100 mM NaF, 20 mM p-Nitrophenyl Phosphate (PNPP), 20 mM  $\beta$ -glycerol phosphate, 50  $\mu$ M sodium vanadate, 0.5 mM phenylmethylsulfonyl fluoride, 2  $\mu$ g/mL aprotinin, 0.5  $\mu$ g/mL leupeptin, 0.7  $\mu$ g/mL pepstatin), followed by the removal of insoluble debris and floating lipids with a bench-top centrifuge at 14 000 rpm at 4°C for 10 minutes to obtain whole protein extracts. The lysate was mixed with SDS loading dye and subjected to sodium dodecyl sulfate polyacrylamide gel electrophoresis (SDS-PAGE) for protein separation. Proteins separated from the gel were transferred to a Polyvinylidene difluoride (PVDF) membrane using a liquid transfer system (Bio-Rad, Hercules, California, USA). The membrane was blocked with 5% nonfat milk in tris-buffered saline and Tween-20 (TBST) ( $\times$ 1 tris-buffered saline (TBS) with 1% Tween-20) for 1 hour at RT and then washed twice with TBST. The membrane was incubated with

a primary antibody for 3 hours at RT or overnight at 4°C with continuous shaking. Primary antibody (anti-Ucp1, ab10983; Abcam, Cambridge, UK; anti-Tubulin, T4026; Sigma-Aldrich, St. Louis, Missouri, USA) solutions were prepared through 1:5000 dilution in 10 mL of  $\times$ 1 TBST containing 3% bovine serum albumin and 0.05%  $NaN_3$ . After incubation with the primary antibody, the membrane was washed in TBST 3 times for 5 minutes each and then incubated in 5% nonfat milk containing a peroxidase conjugated secondary antibody in a ratio of 1:10 000 for 1 hour. The membrane was further washed in TBST 3 times for 30 minutes each. The resultant bands were visualized using Immobilon™ Western Chemiluminescent horseradish peroxidase (HRP) Substrate (Millipore, Burlington, Massachusetts, US), and the total protein loading was visualized through Ponceau S staining of the membrane.

## 2.7 | Histology

Fat specimens were fixed in 0.5% paraformaldehyde (RT15714; Electron Microscopy Sciences, Hatfield, Pennsylvania, US) for 4 to 5 hours and processed with a standard paraffin tissue-embedding protocol. Paraffin-embedded fat tissues were sectioned into 10  $\mu$ m for hematoxylin–eosin staining or 6  $\mu$ m for immunofluorescence staining. Deparaffinization and rehydration were achieved by subjecting sections into 100% xylene, 50% xylene with 50% ethanol, 100% ethanol, 95% ethanol, 70% ethanol subsequently. For hematoxylin–eosin staining, sections were stained with hematoxylin and eosin followed by dehydration in 70% ethanol, 95% ethanol, 100% ethanol, 50% xylene with 50% ethanol and 100% xylene.

## 2.8 | Immunofluorescence staining

0.3% PBST (0.3% Triton in phosphate-buffered saline) was used for all washing steps for fat sections. Samples were blocked with 20% sheep serum in 0.3% PBST for 1 hour. Primary antibody (anti-UCP1, ab10983, 1:200, Abcam, Cambridge, UK) was applied to samples and the samples were kept at 4°C overnight. Samples were then washed 3 times and incubated with an appropriate secondary antibody for 1 hour. The nuclei were counterstained with 100 ng/mL 4',6-diamidino-2-phenylindole. After 3 times washing, the samples were observed under a Nikon Upright fluorescent microscope (Ni-U). Images were captured with a DS-Qi2 Camera (Nikon, Minato, Tokyo, Japan).

# 3 | RESULTS

## 3.1 | Temperature responses of brown and beige fat tissues to NE stimulation

Previous studies have shown that increased NE level can stimulate the thermogenesis of brown adipocytes and the

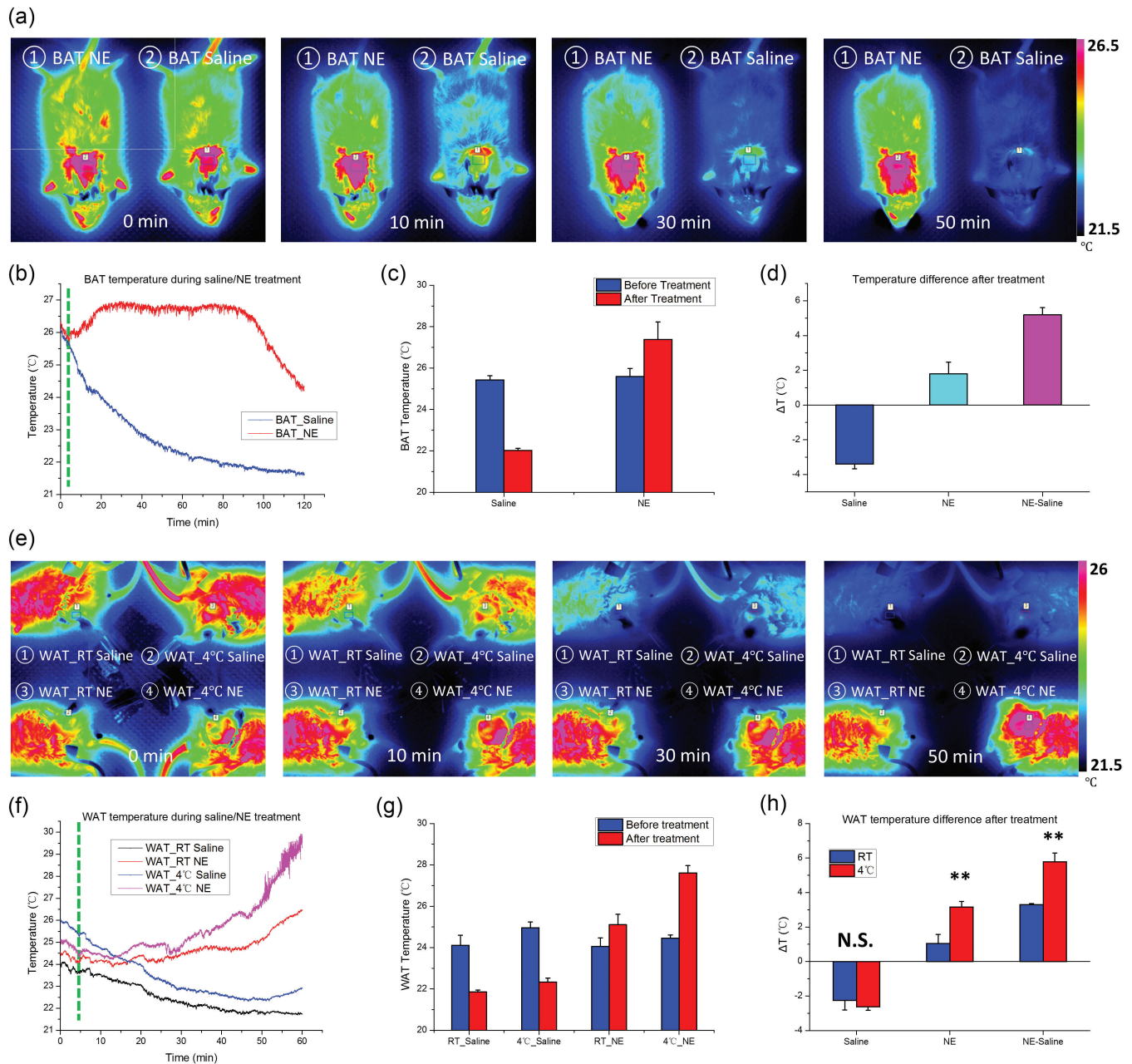


**FIGURE 1** The temperature changes in BAT and WAT during thermogenesis stimulated by NE treatment. A, in vivo thermal imaging of BAT at 0, 10, 30 and 50 minutes after NE (left) and saline (right) injection, respectively. B, The representative temperature profiles of BAT during NE and saline treatment. Green dashed line, time point of NE/saline injection. C, The temperature of BAT tissue measured at 1.5 hours after NE and saline injection, respectively. D, The temperature changes in BAT at 1.5 hours after NE and saline injection, respectively. E, in vivo thermal imaging of WAT of mice kept at RT (left) and at 4°C cold-acclimation (right) at 0, 10, 30 and 50 minutes after NE (bottom) and saline (top) injection, respectively. F, The representative temperature profiles of WAT (RT and 4°C) during NE and saline treatment. Green dashed line, time point of NE/saline injection. G, The temperatures of WAT (RT and 4°C) measured at 1 hour after NE and saline injection, respectively. H, The temperature changes in WAT (RT and 4°C) at 1 hour after NE and saline injection, respectively. Three C57BL6 mice were used for each group in (C–D) and (G–H). \*\* $P < .01$

increased temperature can be used as an indicator of thermogenesis [37, 38]. We used an infrared camera to monitor the temperature change in the interscapular BAT (iBAT) of mice after injection of NE and saline and to assess this thermogenic response process (Figure 1A). Here, the skin in the interscapular region of anesthetized mouse must be surgically removed to allow the temperature of the adipose tissue to be accurately measured (Figure S1). The results show that the local temperature of the BAT increased quickly

upon the injection of NE and remained at a high level for the following 1.5 hours (Figure 1B). In contrast, the BAT temperature of mice with saline treatment decreased continuously due to the cooling effect of anesthetization [39]. The statistical data show that the BAT temperature increased by  $1.8^{\circ}\text{C} \pm 0.7^{\circ}\text{C}$  after NE treatment, while it decreased by  $3.4^{\circ}\text{C} \pm 0.3^{\circ}\text{C}$  in the control group with saline injection (Figure 1C,D). The maximum difference in temperature between NE- and saline-treated mice reached to  $5.2^{\circ}\text{C}$

$\pm 0.4^\circ\text{C}$  (Figure 1D). This result indicates that the thermogenesis of brown adipocytes is well activated through NE treatment, resulting in a significant increase in the local temperature of BAT.

Next, we investigated the thermogenic activity in WAT. We compared the NE-induced temperature change in the iWAT of mice kept at RT and at  $4^\circ\text{C}$  cold-acclimation, a standard approach to induce beige fat inside WAT depot. We found cold-induced WAT browning in all the mice kept at  $4^\circ\text{C}$  (Figure S2). The thermal imaging results show that the local temperature of WAT for mice with or without cold-acclimation treatment rose after NE treatment (Figure 1F). The statistical results indicate that the WAT temperature of mice kept at RT increased by  $1.1^\circ\text{C} \pm 0.5^\circ\text{C}$  an hour after NE injection. The difference in WAT temperature between saline- and NE-treated mice kept at RT was  $3.3^\circ\text{C} \pm 0.1^\circ\text{C}$  (Figure 1G,H). Considering that white adipocytes are incapable to produce heat due to their lack of mitochondrial UCP1, the temperature increase in WAT must be resulted from thermoregulation in which the heat generated in the thermogenic BAT spreads over whole mouse body via blood circulation [1]. However, we indeed found that the WAT of mice kept at  $4^\circ\text{C}$  underwent a greater temperature rise during NE treatment (Figure 1F). The statistical results show that the WAT temperature of mice kept at  $4^\circ\text{C}$  increased by  $3.2^\circ\text{C} \pm 0.3^\circ\text{C}$  after NE injection, and the temperature difference in the browning WAT between saline- and NE-treated mice was  $5.8^\circ\text{C} \pm 0.5^\circ\text{C}$  (Figure 1G,H). This result indicates that the beige adipocytes generated through the cold-induced browning process contribute to the nonshivering thermogenesis, which results in greater local temperature rise in WAT after NE stimulation. The results also demonstrate that the temperature is not an accurate and reliable indicator to study

thermogenesis in browning WAT because the heat generated in BAT raises the temperature in WAT via blood circulation.

### 3.2 | NLO microscopy of adipose tissues in vivo

To investigate the biomorphological and biochemical characteristics of brown and white adipocytes in vivo, we developed a multimodal NLO microscope system of spectroscopic analysis capability to visualize the detailed cellular features of iBAT and iWAT in mice (Figure 2A). This multimodal NLO microscope system integrates femto-second TPEF imaging and picosecond SRS imaging (Figure S3). Specifically, the TPEF imaging reveals mitochondrial activities based on endogenous NADH and FAD fluorescence, while SRS imaging enables the visualization of lipid droplets in adipocytes. Combining TPEF and SRS microscopy, the distribution of mitochondria and morphology of lipid droplets in brown and white adipocytes are clearly revealed. As shown in Figure 2B, the brown adipocytes are enriched with NADH fluorescence emitted from densely packed mitochondria and contain large numbers of small lipid droplets. On the other hand, the white adipocytes with a low abundance of mitochondria contain large lipid droplets surrounded by little cytoplasm. The endogenous fluorescence of BAT and WAT from cytoplasm are dominated by NADH signal under the excitation of 740-nm femto-second laser (Figure 2C), and the SRS spectra of lipids show that the lipid droplets of brown and white adipocytes are dominated by triacylglycerol (Figure 2D) [40].

### 3.3 | ORR measurement

With appropriate excitation, the mitochondrial fluorescence contains the signals from 2 major endogenous fluorophores, NADH and FAD [41, 42]. The fluorescence from these

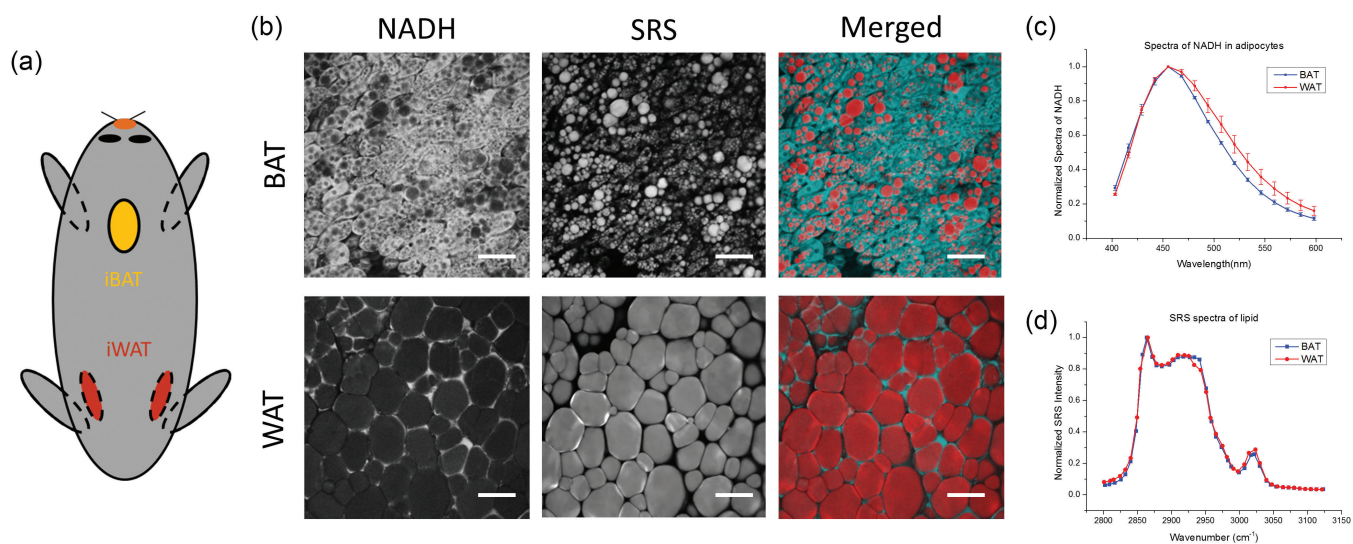


**FIGURE 2** The multimodal NLO imaging of BAT and WAT of mice in vivo. A, Diagram of distribution of iBAT and iWAT in a mouse. B, TPEF and SRS imaging of iBAT and iWAT in vivo. Scale bars: 50  $\mu\text{m}$ . C, Fluorescence spectra measured from the mitochondria in cytoplasmic regions of BAT and WAT. Excitation wavelength: 740 nm. D, SRS spectra of lipid droplets in BAT and WAT

metabolic coenzymes have been widely utilized as intrinsic biomarkers for monitoring cell metabolism [43, 44]. Particularly, the ORR, defined as the ratio of NADH signal peaked at 450 nm to FAD signal peaked at 525 nm, can be used to assess the redox state of tissue [21, 42]. Because NADH and FAD play significant roles in both  $\beta$ -oxidation and ETC [45, 46], we hypothesized that ORR is a sensitive indicator for *in vivo* monitoring the metabolic and thermogenic activities in brown and beige adipocytes during thermogenesis. To simultaneously excite the endogenous fluorescence of NADH and FAD with a single wavelength, the femtosecond laser was tuned at 810 nm, an optimal wavelength to ensure well-balanced 2-photon excitation efficiencies of NADH and FAD for ORR measurement [19, 47]. Since our TPEF microscope record images in 16 wavelength channels simultaneously, we first extracted the TPEF spectra from the cytoplasm of adipocytes in the imaged BAT and WAT based on the intensity contrast between mitochondria and lipid fluorescence. This imaging-guided spectroscopy method for the extraction of TPEF spectral signal has been described previously [48]. As shown in Figure 3A, the cytoplasmic fluorescence spectra of both brown and white adipocytes exhibit similar line shape, a typical combination of balanced NADH and FAD fluorescence [47]. Applying the imaging-guided spectroscopy analysis to lipid droplets, a weak fluorescence with peak blue-shifted to 445 nm were observed as shown in Figure 3A. As reported by other groups, the intrinsic fluorescence in lipid droplets may arise from lipid oxidation products [28, 49]. In this work, we calculated ORRs based on the ratio of mitochondrial TPEF signals recorded in 446- and 459-nm channels to the signals in 524- and 537-nm channels. As shown in Figure 3B, there is no significant difference in cytoplasmic ORRs between brown and white adipocytes, while the corresponding ratio calculated from the lipid droplet fluorescence is much greater than ORRs in both BAT and WAT due to the blue-shifted fluorescence spectrum of lipid droplets.

Next, we investigated the dynamic metabolism of adipose tissues using the *in vivo* ORR detection technique. First, we measured the ORRs from the TPEF spectral images of BAT after NE and saline treatment, respectively. The results show that the ORRs of the brown adipocytes rose rapidly after NE injection, while ORR remained stable for mice with saline injection (Figure 3C). The dynamic change in the ORR of BAT is consistent with the biochemical transformation of NE-induced fatty acid  $\beta$ -oxidation, in which NADH is produced and FAD is consumed through reduction reactions, leading to a rapid rise in ORR. The gradual decrease of ORR at 20 minutes after NE stimulation may be due to the restore of mitochondrial proton gradient via oxidative phosphorylation that consumes NADH and produces FAD. Meanwhile, the rise in the NADH/NAD<sup>+</sup> or acetyl-CoA/CoA ratios may also result in feedback inhibition of fatty acid  $\beta$ -oxidation and thus lead to the gradual

decrease of ORR [50, 51]. When the ORR measurement was conducted in WAT, we found that the ORRs of cytoplasm in WAT remained stable after NE and saline treatment (Figure 3D). This indicates that WAT is metabolically inactive and the adrenergically stimulated thermogenesis does not take place in white adipocytes. Moreover, we analyzed the intrinsic fluorescence of lipid droplets in WAT. As shown in Figure 3E, the fluorescence of lipid droplets was also not affected by the NE and saline treatment. The results indicate that ORR is a sensitive and reliable biomarker for quantitative monitoring the metabolic status of adipocytes during thermogenic processes *in vivo*.

### 3.4 | Measurement of thermogenesis in deep tissues

Although TPEF imaging can reveal detailed morphological and metabolic characteristics of adipocytes, its imaging depth is limited to 80 to 100  $\mu$ m because of the optical heterogeneity caused by numerous lipid droplets [52, 53]. This imaging depth limitation was previously reported in the 2-photon imaging of lipid-abundant tissues [28, 54]. Our findings showed that beige fat is highly heterogeneously produced within the WAT depot (Figure S2A). We did not observe the cold-induced beige fat cells on the superficial WAT by using the integrated 2-photon fluorescence and SRS microscope due to limited imaging depth. Therefore, a tool for metabolic assessment in the deep tissue is a necessity to study the thermogenesis of beige fat in deep WAT sites. In this work, we developed a compact fiber-based spectroscopy system for the measurement of ORRs over a large volume of adipose tissues *in vivo*. As shown in the schematic diagram in Figure 4A, we used a 405-nm laser for simultaneous single-photon excitation of NADH and FAD fluorescence [19, 47]. The optical fiber bundle was made up of 7 single fibers (Figure S4), enabling the robust and high-efficiency *in vivo* detection of the fluorescence in biological tissues. Specifically, a single source fiber in the center delivered 405-nm excitation to tissue and the surrounding 6 fibers collected the backscattered fluorescence for real-time ORR detection (Figure 4B). The collection fibers were rearranged into linear arrays to conduct the fluorescence signal into a spectrograph equipped with 16-channel PMT arrays for spectral analysis. This fiber catheter produces a laser spot of 0.5-mm diameter at the tissue surface, and the corresponding detector area is about 0.8 mm<sup>2</sup> (Figure S4). We calculated the radiant fluence map inside adipose tissue using a Monte Carlo simulation based on the optical properties of adipose tissue at 405 nm [33]. As shown in Figure 4C, the optical penetration depth of the source photons was about 0.81 mm and the volume of tissue illuminated with over 10% of peak intensity is around 0.33 mm<sup>3</sup>, demonstrating that this easy-to-use fiber-based spectroscopy enables quantitative assays of the fluorescent properties in adipose tissues much deeper than multiphoton microscopy. For *in vivo* ORR measurement, the exact fat

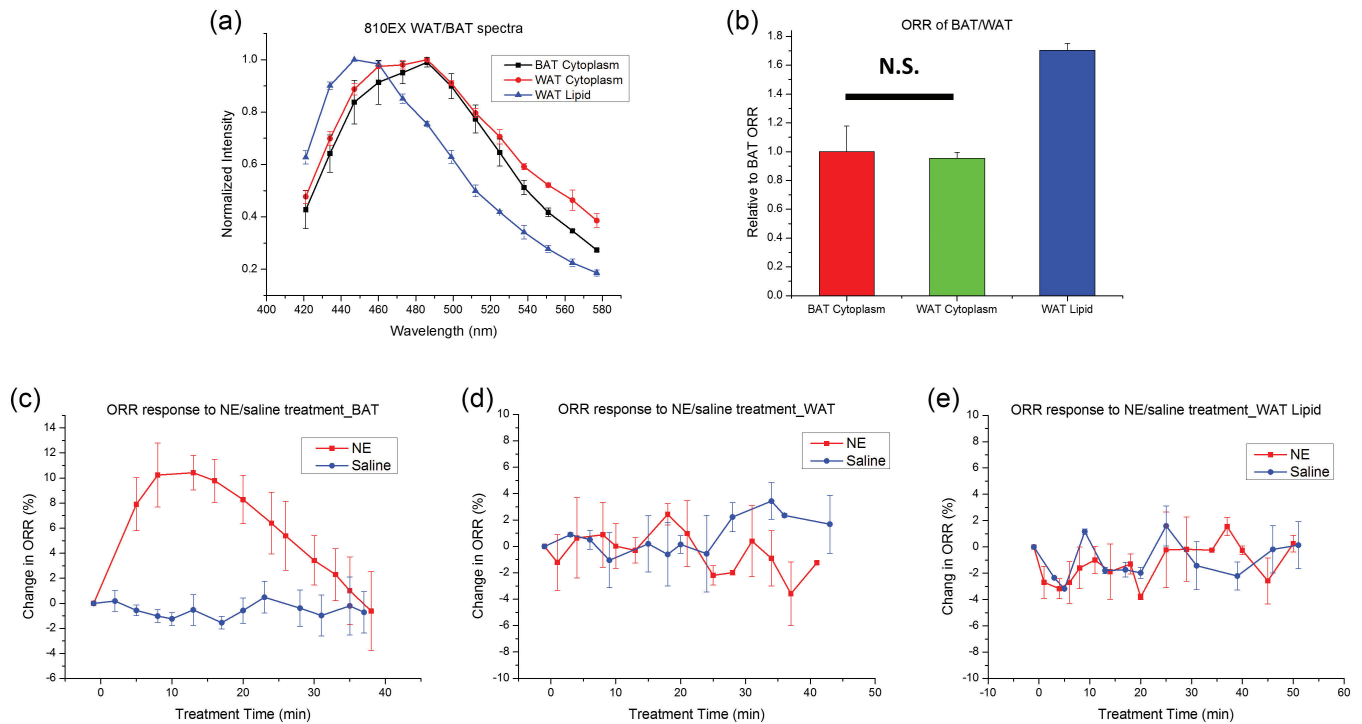


**FIGURE 3** Analysis of the ORR of brown and white adipocytes. A, TPEF spectra measured from cytoplasm and lipid droplets of brown and white adipocytes, respectively. B, Relative ORRs in adipose tissues and corresponding ratio in lipid droplets. C, Change in the cytoplasmic ORRs of BAT during NE and saline treatment in vivo. D, Change in the cytoplasmic ORRs of WAT during NE and saline treatment in vivo. E, Change in the corresponding ratio of lipid droplets in WAT during NE and saline treatment in vivo. Each statistical data in (A-E) is shown in terms of its average with its SD over the measurements from 3 mice. The ORRs are the average values measured from all adipocytes in a  $400\ \mu\text{m} \times 400\ \mu\text{m}$  field of view

volume will be influenced by the heterogeneous distribution of lipid droplets, which could cause diverse absorption and scattering properties inside the examined adipose tissues. However, it should be noted that the measured signals are the total fluorescence from cytoplasm and lipid droplets because the fiber probe-based measurement does not provide selectivity of subcellular features.

We studied the fluorescence spectral signals from BAT and WAT of mice kept at RT and at  $4^\circ\text{C}$  cold-acclimation, respectively. As shown in Figure 4D, the total fluorescence of BAT was peaked at 498 nm because the NADH and FAD fluorescence in BAT cytoplasm are the dominant autofluorescence signals. The peak of WAT fluorescence measured from the mice kept at RT blue-shifted to 459 nm, which is due to the autofluorescence of large lipid droplets in white adipocytes. An important finding is that the fluorescence spectrum of the WAT of mice kept at  $4^\circ\text{C}$  cold-acclimation is peaked at 472 nm, redshifted with respect to the WAT fluorescence from the mice kept at RT. This spectral shift is due to the induction of beige adipocytes which have much larger amount of cytoplasmic mitochondria and smaller lipid droplets in comparison with white adipocytes. The results suggest that the beige adipocytes in cold-acclimated mice and the degree of WAT browning could be identified spectroscopically.

Next, we recorded the fluorescence signals in BAT during the NE-induced thermogenesis. As shown in Figure 4E, the fluorescence spectrum of BAT peaked at 498 nm blue-

shifted to 485 nm after NE injection due to rapid NADH production and FAD consumption via  $\beta$ -oxidation. In contrast, no spectral shift was observed in the group with saline treatment (Figure 4F). The ORR in BAT increased rapidly within 5 minutes after NE injection and remained at a high level for about an hour, while the ORRs remained unchanged throughout the entire period in the group of saline treatment (Figure 4G). The dramatic increase in ORR indicates the rapid and strong response of brown adipocytes to NE treatment. In comparison with the temperature measured in BAT after NE treatment, the dynamic changes of ORR and temperature are strongly correlated as shown in Figure 4H. However, the ORR rises much more quickly than temperature after NE treatment because it indicates biochemical response to the stimulation. The ORR starts to drop about 40 minutes after NE treatment due to the restore of mitochondrial proton gradient through oxidative phosphorylation which consumes NADH and produces FAD. Statistically, we found that the NE treatment induced  $31.6\% \pm 6.5\%$  increase in ORR of BAT (Figure 4I). We also noticed that the NE-stimulated change in ORR measured in deep BAT via fiber-based spectroscopy system, in terms of amplitude and rising slope, is higher than that measured from the surface of BAT by TFPE microscope. The difference may be due to that the local temperature at the tissue surface was lower, and the cellular metabolism and viability are sensitive to temperature [55, 56].

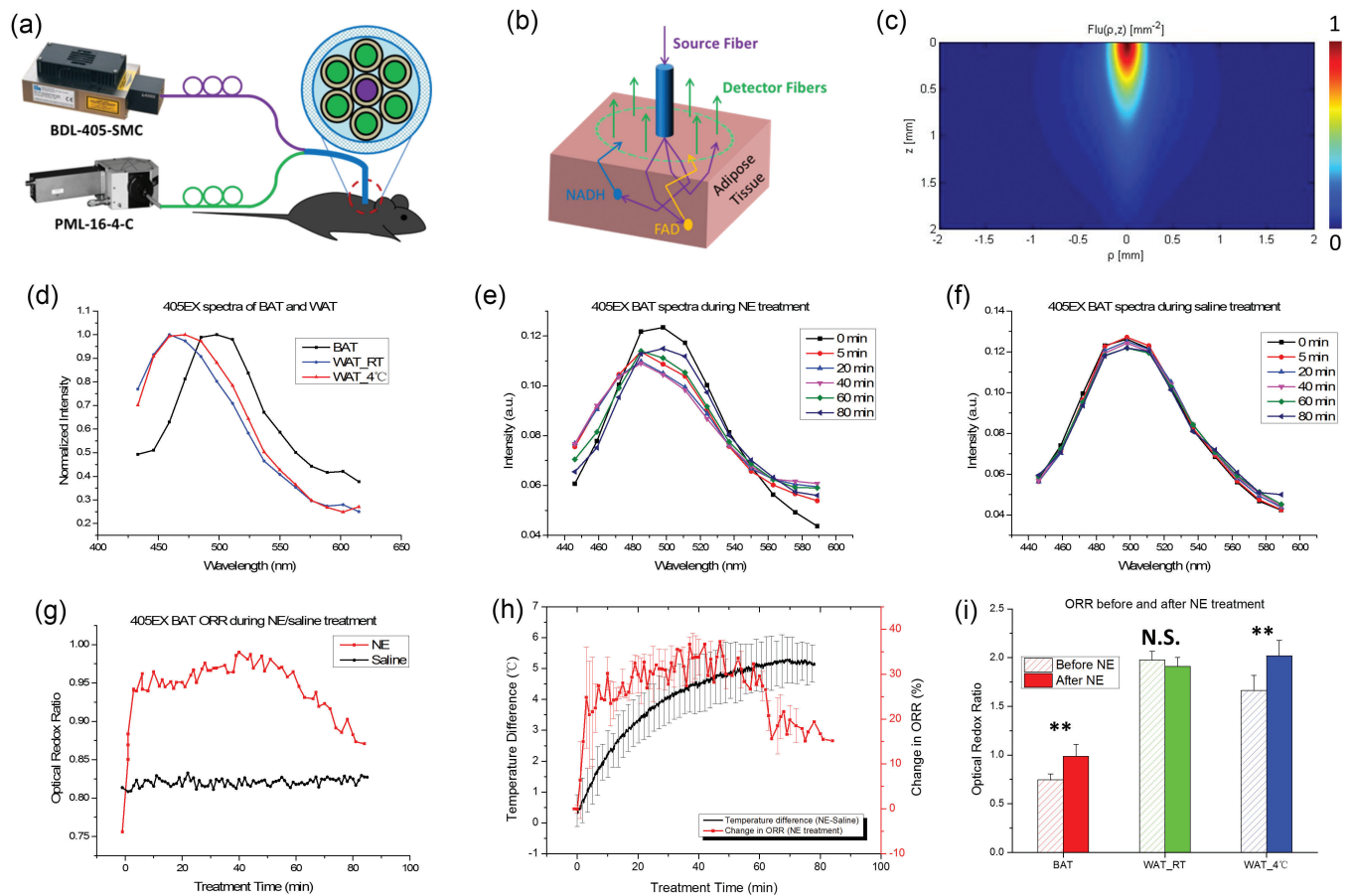


**FIGURE 4** Thermogenic responses of deep adipose tissues in vivo. A, Schematic diagram of a fiber-based spectroscopy system used to measure ORR change of deep adipose tissues. A 405-nm laser (BDL-405-SMC) was used as the excitation source. The autofluorescence was excited and collected through the same fiber bundle. A spectrograph equipped with a 16-channel PMT array (PML-16-4-C) was used for spectral analysis. B, Excitation and collection geometry of the fiber bundle. C, Monte Carlo simulation of photon transport in adipose tissue phantom. The intensity of fluence was normalized in the simulation area (2 mm × 4 mm). D, Fluorescence spectra of different types of adipose tissues excited with the 405-nm laser. E, Fluorescence spectra of BAT during NE treatment. F, Fluorescence spectra of BAT after saline injection. G, ORRs of BAT during NE/saline treatment. H, Temporal correlation between dynamic changes in ORRs and temperature during NE treatment. The black line shows the change in temperature differences of BAT between NE- and saline-treated mice. The red line shows the change in ORR of BAT during NE-stimulated thermogenesis. Each statistical curve is shown in terms of its average with its SD over the measurements from 3 mice. I, ORRs of BAT, WAT and browning WAT before (open bars) and after (solid bars) NE treatment. \*\* $P < .01$

In the study of metabolic characteristics of WAT, we measured changes in the ORR of WAT of mice kept at RT and at 4°C cold-acclimation during the thermogenic process. As pointed out previously, the measured signals from WAT using fiber bundle probe are the total fluorescence from both cytoplasm and lipid droplets of adipocytes in a large tissue volume. The calculated basal ORRs of WAT are much greater than those of BAT (Figure 4I), which is attributed to the autofluorescence of large lipid droplets in white adipocytes. The basal ORRs of WAT from the mice kept at 4°C were found to be lower than those kept at RT, due to the mitochondria-abundant beige adipocytes acquired in WAT after cold-acclimation. Moreover, the sampling volume is determined by the optical properties of fat tissue, particularly the scattering coefficient because the absorption in fat tissue is small [33]. The morphology of cold-induced beige fat cells is between white and brown adipocytes, and the lipid droplet sizes in beige fat cells are much smaller

than that in the white adipocytes. Therefore, the scattering coefficient of browning WAT is different from that of pure WAT. The scattering coefficient is also dependent on the degree of browning or the density of beige fat cells in the browning WAT. The variation of scattering in browning WAT will change the volume explored by the fiber probe and the ORR value. This may also contribute to that the basal ORRs measured from the browning WAT spread over a relatively broad range. However, it should be emphasized that the thermogenic response of browning WAT is measured by the relative change in ORR before and after NE stimulation. Thus, the variation of scattering in the browning WAT should not affect the measurement results. The study on NE response shows that unlike temperature measurement, the ORRs of the WAT of mice kept at RT remained unchanged during NE treatment (Figure 4I). On the other hand, the ORRs of WAT of mice kept at 4°C increased by  $23.5\% \pm 18.3\%$  after NE treatment, exhibiting

similar characteristics as BAT (Figure 4I). In the control groups, the ORRs of WAT in all mice remained stable during the treatment with saline. These results demonstrated that the beige adipocytes in the WAT induced by cold-acclimation contribute to the local thermogenesis stimulated by NE treatment. The findings demonstrate that the ORR is a more sensitive and reliable label-free biomarker than temperature for monitoring the thermogenesis of beige adipocytes in WAT.

### 3.5 | Correlation of ORRs and WAT browning

As shown in Figure 4I, the basal ORRs measured in the browning WAT of cold-acclimated mice are between those measured in BAT and WAT. The wide range distribution of ORRs in browning WAT is due to heterogeneity in the induction of UCP1-expressing beige adipocytes in WAT or variations in the degree of WAT browning. Therefore, basal ORRs could provide a quantitative indicator to evaluate the degree of WAT browning that is directly correlated to the thermogenic capacity of browning WAT. Because the expression of UCP1 is a key factor to determine the ability of adipose tissue to dissipate energy, we studied the correlation between basal ORR and UCP1 expression from the same WAT of cold-acclimated mice. In detail, we measured the ORR at different sites of WAT depots using fiber-based spectroscopy system, and biopsies were then taken from the exactly same sites where ORR measurements were performed. Next, Western blotting was used to determine the UCP1 content in each biopsied sample. The UCP1 expressions of biopsies taken from a single WAT depot of the same mouse are shown in Figure 5A. As can be seen, only 2 out of 6 biopsy samples are UCP1 positive, indicating that the WAT browning is highly heterogeneous even within a single WAT depot. However, the statistical results based on the measurements from 3 mice clearly demonstrate that the ORRs of UCP1-positive WAT are significantly lower than those of WAT with low UCP1 expression (Figure 5B). Two outliers could be from the poor spatial resolution of biopsy procedure. Furthermore, we analyzed the correlation between the basal ORR of the WAT of cold-acclimated

mice and the absolute change of ORR after the NE stimulation. A significant Pearson correlation was found between the basal ORRs and NE responses in individual mice (Figure 5C,  $r = -0.851$ ,  $p = .007$ ). The results show that WAT with lower ORRs exhibit a greater thermogenic response to NE stimulation because increased value of ORR is the indicator of thermogenic capacity. This is consistent with our findings that adipose tissues with lower ORRs have a higher level of UCP1 expression. The results provide evidences to confirm that the basal ORRs of local adipose tissue can serve as a label-free indicator for in vivo and real-time measurement of degree of WAT browning.

## 4 | DISCUSSION

In this study, high-resolution TPEF spectral imaging and SRS imaging were used to visualize the morphological and biochemical characteristics of the adipocytes in BAT and WAT in vivo. We found that the ORR based on NADH and FAD fluorescence is a label-free biomarker to characterize the metabolism of brown adipocytes during NE-stimulated thermogenesis in mice. However, the optical heterogeneity in adipose tissues limits the penetration depth of NLO imaging. To assess the metabolic activity in deep adipose tissues in vivo, we developed a compact fiber-based spectroscopy system to measure the ORR from a large volume of tissue. The ORR in BAT increased significantly during NE-stimulated thermogenesis, while no change in ORR was found in WAT during the stimulation. The results demonstrate that the label-free ORR measurement can accurately capture the highly dynamic change of redox state in adipocytes during the intense thermogenesis induced by NE. In the study of cold-acclimated mice, we discovered that the basal ORR of WAT is closely related to the degree of WAT browning. Specifically, low basal ORR value of browning WAT corresponds to a high UCP1 expression in browning WAT and to an enhanced thermogenic response to NE stimulation. Therefore, the basal ORR in browning WAT also serves as a biomarker to characterize its thermogenic capabilities.

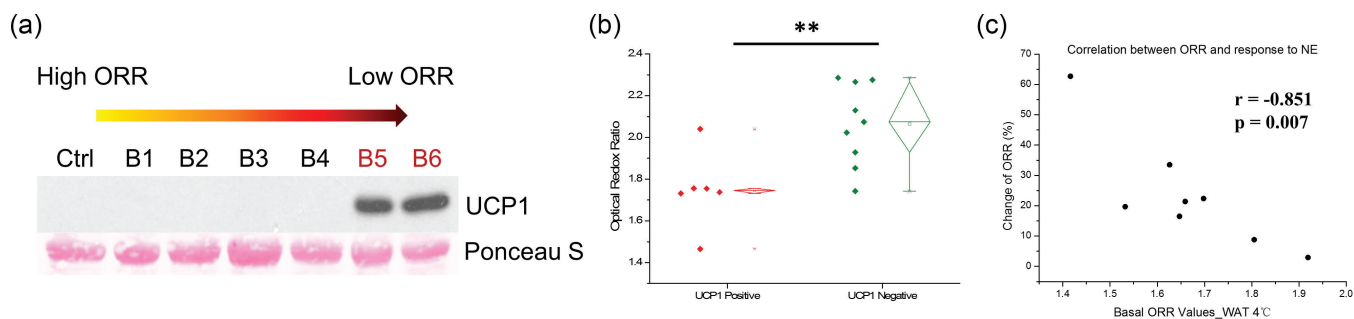


**FIGURE 5** The correlation between ORR and UCP1 expression in WAT of cold-acclimated mice. A, UCP1 protein expression in biopsy samples taken from a single white adipose depot. The sequence of biopsy samples (B1-B6) is arranged from highest to lowest ORR. B, Statistics of ORRs of UCP1-positive and negative biopsy samples. The data were collected from 3 cold-acclimated mice.  $**P < .01$ . C, Correlation between basal ORRs and changes of ORRs induced by NE in WAT of 8 cold-acclimated mice. Pearson coefficient and corresponding  $P$ -value are shown

The conventional approaches of *in vivo* quantification of thermogenesis, including the measurements of oxygen consumption or blood flow, locomotor activity and food intake, are mainly based on indirect assessments on the metabolism of whole animal. These techniques do not provide information on the thermogenesis of specific brown or WAT. Furthermore, recent study showed that after NE stimulation, the increases of blood flow in BAT and oxygen consumption rate in whole mouse are not always related to UCP1 expressions in brown and beige adipocytes, indicating that the measurements of blood flow and oxygen consumption may not provide accurate estimation on the thermogenesis in BAT or browning WAT [57, 58]. Finally, although thermal imaging allows the noninvasive measurement of temperature changes in BAT, our results show that the heat locally produced in BAT can quickly redistribute throughout the animal body via blood circulation and raise the temperature in WAT. This can result in overestimation of the thermogenic capability of browning WAT. In addition, the comparison of NE-stimulated rise in ORR with temperature demonstrates that the ORR responds the stimulation more quickly than temperature (Figure 4H) and can capture the rapid dynamics of thermogenesis at early stage. It also should be noted that the compact spectroscopy measurement is based on a highly robust fiber probe with fixed measurement geometry. It can be applied to awake mouse that is not under anesthesia as in the study of optogenetic manipulation of neural activity [59, 60]. The long-term measurements on awake animal can provide more rigorous information on a variety of biological processes, such as thermogenic and metabolic activities in adipose tissues. Combined with potential approaches to recruit and activate brown or beige fat in human body, this label-free and real-time metabolic monitoring system may be applied in translational research to assess the development and function of the thermogenic adipocytes in human and thus may help to develop therapeutic strategies against obesity.

#### ACKNOWLEDGMENTS

This work was supported by the Hong Kong Research Grants Council through grants 662513, 16103215, 16148816, T13-607/12R T13-706/11-1 and AOE/M-09/12 and Hong Kong University of Science & Technology (HKUST) through grant RPC10EG33.

#### Author contributions

J.Y.Q. and Z.W. designed the experimental schemes and supervised the project. S.H., X.L., Q.S. and J.Y.Q. developed the microscope and spectroscopy system. S.H., Y.A. and X.W. designed and performed experiments. S.H., Y.A. and J.Y.Q. wrote the manuscript with inputs from all authors.

#### Conflict of interest

The authors declare no potential conflict of interests.

#### AUTHOR BIOGRAPHIES

Please see Supporting Information online.

#### REFERENCES

- [1] B. Cannon, J. Nedergaard, *Physiol. Rev.* **2004**, *84*, 277.
- [2] B. B. Lowell, V. S-Susulic, A. Hamann, J. A. Lawitts, J. Himms-Hagen, B. B. Boyer, L. P. Kozak, J. S. Flier, *Nature* **1993**, *366*, 740.
- [3] Y. Kontani, Y. Wang, K. Kimura, K. Inokuma, M. Saito, T. Suzuki-Miura, Z. Wang, Y. Sato, N. Mori, H. Yamashita, *Aging Cell* **2005**, *4*, 147.
- [4] I. Shimomura, R. E. Hammer, J. A. Richardson, S. Ikemoto, Y. Bashmakov, J. L. Goldstein, M. S. Brown, *Genes Dev.* **1998**, *12*, 3182.
- [5] M. Harms, P. Seale, *Nat. Med.* **2013**, *19*, 1252.
- [6] A. M. Cypess, S. Lehman, G. Williams, I. Tal, D. Rodman, A. B. Goldfine, F. C. Kuo, E. L. Palmer, Y. H. Tseng, A. Doria, G. M. Kolodny, C. R. Kahn, *N. Engl. J. Med.* **2009**, *360*, 1509.
- [7] M. Saito, Y. Okamatsu-Ogura, M. Matsushita, K. Watanabe, T. Yoneshiro, J. Nio-Kobayashi, T. Iwanaga, M. Miyagawa, T. Kameya, K. Nakada, Y. Kawai, M. Tsujisaki, *Diabetes* **2009**, *58*, 1526.
- [8] W. D. van Marken Lichtenbelt, J. W. Vanhommerig, N. M. Smulders, J. M. Drossaerts, G. J. Kemerink, N. D. Bouvy, P. Schrauwen, G. J. Teule, *N. Engl. J. Med.* **2009**, *360*, 1500.
- [9] K. A. Virtanen, M. E. Lidell, J. Orava, M. Heglind, R. Westergren, T. Niemi, M. Taittonen, J. Laine, N. J. Savisto, S. Enerbäck, P. Nuutila, *N. Engl. J. Med.* **2009**, *360*, 1518.
- [10] J. Wu, P. Boström, L. M. Sparks, L. Ye, J. H. Choi, A. Giang, M. Khandekar, K. A. Virtanen, P. Nuutila, G. Schaart, K. Huang, H. Tu, W. D. van Marken Lichtenbelt, J. Hoeks, S. Enerbäck, P. Schrauwen, B. M. Spiegelman, *Cell* **2012**, *150*, 366.
- [11] J. Wu, P. Cohen, B. M. Spiegelman, *Genes Dev.* **2013**, *27*, 234.
- [12] W. Wang, P. Seale, *Nat. Rev. Mol. Cell Biol.* **2016**, *17*, 691.
- [13] A. Fedorenko, P. V. Lishko, Y. Kirichok, *Cell* **2012**, *151*, 400.
- [14] B. Cannon, J. Nedergaard, *J. Exp. Biol.* **2011**, *214*, 242.
- [15] S. Virtue, A. Vidal-Puig, *Front. Physiol.* **2013**, *4*, 128.
- [16] A. Matthias, K. B. Ohlson, J. M. Fredriksson, A. Jacobsson, J. Nedergaard, B. Cannon, *J. Biol. Chem.* **2000**, *275*, 25073.
- [17] J. Ukropec, R. P. Anunciado, Y. Ravussin, M. W. Hulver, L. P. Kozak, *J. Biol. Chem.* **2006**, *281*, 31894.
- [18] W. R. Zipfel, R. M. Williams, W. W. Webb, *Nat. Biotechnol.* **2003**, *21*, 1369.
- [19] Y. Wu, J. Y. Qu, *Opt. Lett.* **2006**, *31*, 1833.
- [20] Y. Wu, P. Xi, J. Y. Qu, T. Cheung, M. Yu, *Opt. Express* **2005**, *13*, 382.
- [21] J. H. Ostrander, C. M. McMahon, S. Lem, S. R. Millon, J. Q. Brown, V. L. Seewaldt, N. Ramanujam, *Cancer Res.* **2010**, *70*, 4759.
- [22] A. J. Walsh, R. S. Cook, M. E. Sanders, L. Aurisicchio, G. Ciliberto, C. L. Arteaga, M. C. Skala, *Cancer Res.* **2014**, *74*, 5184.
- [23] Y. Wu, J. Y. Qu, *J. Biomed. Opt.* **2006**, *11*, 054023.
- [24] W. L. Rice, D. L. Kaplan, I. Georgakoudi, *PLoS One* **2010**, *5*, e10075.
- [25] J. Hou, H. J. Wright, N. Chan, R. Tran, O. V. Razorenova, E. O. Potma, B. J. Tromberg, *J. Biomed. Opt.* **2016**, *21*, 060503.
- [26] S. M. Houten, R. J. Wanders, *J. Inherit. Metab. Dis.* **2010**, *33*, 469.
- [27] M. Calderon-Dominguez, J. F. Mir, R. Fucho, M. Weber, D. Serra, L. Herrero, *Adipocyte* **2016**, *5*, 98.
- [28] C. A. Alonzo, S. Karaliota, D. Pouli, Z. Liu, K. P. Karalis, I. Georgakoudi, *Sci. Rep.* **2016**, *6*, 31012.
- [29] J. Nedergaard, B. Cannon, *Biochim. Biophys. Acta* **2013**, *1831*, 943.
- [30] K. Czamara, K. Majzner, M. Z. Pacia, K. Kochan, A. Kaczor, M. Baranska, *J. Raman Spectrosc.* **2015**, *46*, 4.
- [31] P. Wang, M. N. Slipchenko, B. Zhou, R. Pinal, J. Cheng, *IEEE J. Sel. Top. Quant. Electron.* **2012**, *18*, 384.
- [32] M. Balu, A. Mazhar, C. K. Hayakawa, R. Mittal, T. B. Krasieva, K. König, V. Venugopalan, B. J. Tromberg, *Biophys. J.* **2013**, *104*, 258.
- [33] A. Bashkatov, E. Genina, V. Kochubey, V. Tuchin, *Opt. Spectrosc.* **2005**, *99*, 836.

- [34] J. Ritz, A. Roggan, C. Isbert, G. Müller, H. J. Buhr, C. Germer, *Lasers Surg. Med.* **2001**, *29*, 205.
- [35] J. M. Stujenske, T. Spellman, J. A. Gordon, *Cell Rep.* **2015**, *12*, 525.
- [36] G. Yona, N. Meitav, I. Kahn, S. Shoham, *eNeuro* **2016**, *3*, ENEURO.0059-15.2015.
- [37] J. D. Crane, E. P. Mottillo, T. H. Farncombe, K. M. Morrison, G. R. Steinberg, *Mol. Metab.* **2014**, *3*, 490.
- [38] T. J. Schulz, P. Huang, T. L. Huang, R. Xue, L. E. McDougall, K. L. Townsend, A. M. Cypess, Y. Mishina, E. Gussoni, Y. H. Tseng, *Nature* **2013**, *495*, 379.
- [39] A. C. Caro, F. C. Hankenson, J. O. Marx, *J. Am. Assoc. Lab. Anim. Sci.* **2013**, *52*, 577.
- [40] D. Fu, Y. Yu, A. Folick, E. Currie, R. V. Farese Jr., T. Tsai, X. S. Xie, M. C. Wang, *J. Am. Chem. Soc.* **2014**, *136*, 8820.
- [41] S. Huang, A. A. Heikal, W. W. Webb, *Biophys. J.* **2002**, *82*, 2811.
- [42] M. C. Skala, K. M. Riching, A. Gendron-Fitzpatrick, J. Eickhoff, K. W. Eliceiri, J. G. White, N. Ramanujam, *Proc. Natl. Acad. Sci. U. S. A.* **2007**, *104*, 19494.
- [43] Y. Wu, W. Zheng, J. Y. Qu, *Opt. Lett.* **2006**, *31*, 3122.
- [44] M. Skala, N. Ramanujam, in *Advanced Protocols in Oxidative Stress II* (Ed: D. Armstrong), Humana Press: Totowa, New Jersey, **2010**, p. 155.
- [45] H. Schulz, *Metabolism* **1991**, *1081*, 109.
- [46] A. R. Fernie, F. Carrari, L. J. Sweetlove, *Curr. Opin. Plant Biol.* **2004**, *7*, 254.
- [47] Y. Wu, J. Y. Qu, *Opt. Lett.* **2005**, *30*, 3045.
- [48] S. He, C. Ye, Q. Sun, C. K. Leung, J. Y. Qu, *Biomed. Opt. Express* **2015**, *6*, 1055.
- [49] R. Datta, A. Alfonso-Garcia, R. Cinco, E. Gratton, *Sci. Rep.* **2015**, *5*, 9848.
- [50] H. Schulz, *J. Nutr.* **1994**, *124*, 165.
- [51] S. Eaton, *Prog. Lipid Res.* **2002**, *41*, 197.
- [52] D. N. Nikogosyan, *Properties of Optical and Laser-related Materials: A Handbook*, Wiley-VCH: Weinheim, Germany, **2003**, p. 614. ISBN: ISBN 0-471-97384-X.
- [53] K. Kim, S. Lee, J. Yoon, J. Heo, C. Choi, Y. Park, *Sci. Rep.* **2016**, *6*, 36815.
- [54] M. J. Farrar, I. M. Bernstein, D. H. Schlafer, T. A. Cleland, J. R. Fetcho, C. B. Schaffer, *Nat. Methods* **2012**, *9*, 297.
- [55] E. Trummer, K. Fauland, S. Seidinger, K. Schriebl, C. Lattenmayer, R. Kunert, K. Vorauer-Uhl, R. Weik, N. Borth, H. Katinger, D. Müller, *Biotechnol. Bioeng.* **2006**, *94*, 1033.
- [56] M. Vergara, S. Becerra, J. Berrios, N. Osses, J. Reyes, M. Rodríguez-Moyá, R. Gonzalez, C. Altamirano, *PLoS One* **2014**, *e93865*, 9.
- [57] G. Abreu-Vieira, C. E. Hagberg, K. L. Spalding, B. Cannon, J. Nedergaard, *Am. J. Physiol. Endocrinol. Metab.* **2015**, *308*, E822-9.
- [58] H. M. Feldmann, V. Golozoubova, B. Cannon, J. Nedergaard, *Cell Metab.* **2009**, *9*, 203.
- [59] K. Ung, B. R. Arenkiel, *JoVE* **2012**, *68*, e50004.
- [60] M. M. Sidor, T. J. Davidson, K. M. Tye, M. R. Warden, K. Diesseroth, C. A. McClung, *JoVE* **2015**, *95*, 51483.

## SUPPORTING INFORMATION

Additional Supporting Information may be found online in the supporting information tab for this article.

**Figure S1.** *in vivo* thermal imaging of BAT without surgical removal of interscapular skin. A, Thermal image of mice before NE and saline injection. B, Thermal image of mice at 30 minutes after NE (left) and saline (right) injection. C, Temperature change at iBAT region during NE and saline treatment.

**Figure S2.** Cold-induced browning of iWAT. A, H&E staining images show that beige adipocytes with smaller lipid droplets were largely found in iWAT of mice kept at 4°C. B, The immunostaining of the UCP1 expression (red) shows that the protein abundance of UCP1 in WAT of cold-acclimated mice was significantly higher than that of mice kept at RT. Scale bars: 100 µm. C, Western blotting results for WAT of mice kept at RT and at 4°C. Tubulin was used as a control protein in the analysis. Three mice were used in each group.

**Figure S3.** Optical layout and block diagram of the multimodal NLO microscope system. A, Multimodal NLO microscope system integrates TPEF and SRS imaging. HWP, half-wave plate; PBS, cube polarizing beam splitter; DM, dichroic mirror for TPEF imaging; the DM and PBS are interchangeable above the objective through a motorized flip mount to achieve TPEF and SRS imaging sequentially. Fs, filter set; SP, short-pass filter; FB, fiber bundle; M-PMT, multichannel photomultiplier tube; PD, photodiode. B, Setup of *in vivo* multimodal NLO imaging of BAT.

**Figure S4.** Geometry of the distal tip of fiber bundle. A, The distal tip of the fiber bundle shows the central source fiber (purple) and 6 surrounding detector fibers (green). The refractive index of the 1-mm quartz window at the end of the distal tip matches that of the optical fibers. During the measurement of fluorescence signals, the distal tip was gently placed in contact with the tissue surface. A, 0.5-mm-diameter laser spot was produced at the end of the sensor, and the diameter of the collection area was 1 mm. B, Geometry of the source and detector fibers. The radius of fiber ( $r_0$ ) was 100 µm and the distance between the central source fiber and the detector fiber ( $r_1$ ) was 250 µm.

**How to cite this article:** He S, An Y, Li X, et al. *In vivo* metabolic imaging and monitoring of brown and beige fat. *J. Biophotonics*. 2018;e201800019. <https://doi.org/10.1002/jbio.201800019>